



Trilayer CdS/carbon nanofiber (CNF) mat/Pt-TiO₂ composite structures for solar hydrogen production: Effects of CNF mat thickness

Young Kwang Kim^a, Sang Kyoo Lim^a, Hyunwoong Park^b, Michael R. Hoffmann^c, Soonhyun Kim^{a,*}

^a Division of Nano and Energy Convergence Research, Daegu Gyeongbuk Institute of Science and Technology (DGIST), Daegu, 42988, Republic of Korea

^b School of Energy Engineering, Kyungpook National University, Daegu 41566, Republic of Korea

^c Linde + Robinson Laboratories, California Institute of Technology (CALTECH), Pasadena, CA 91125, United States

ARTICLE INFO

Article history:

Received 29 February 2016

Received in revised form 27 April 2016

Accepted 20 May 2016

Available online 20 May 2016

Keywords:

Photocatalytic water splitting

Carbon nanomaterial

Composite catalyst

Electron-transfer mediation

ABSTRACT

Solar H₂ production by photocatalytic water splitting is a promising technology that permits direct H₂ production from the clean and abundant resources of water and solar light. We successfully fabricated trilayer heterostructures of CdS/carbon nanofiber (CNF) mat/Pt-deposited TiO₂ (Pt-TiO₂) for solar H₂ production. The CNF mat was prepared by electrospinning and carbonization. CdS and Pt-TiO₂ were coated on the front and back of the CNF mat by doctor blading. Under visible-light irradiation on the CdS side, the addition of the Pt-TiO₂ coating improved the H₂ production by a factor of 3.4. This suggests that the H₂ production reaction could occur on Pt-TiO₂, which is not active under visible irradiation; therefore, the CNF mat could act as an efficient photogenerated electron-transfer mediator from CdS to Pt-TiO₂. The H₂ production rates of the trilayer CdS/CNF/Pt-TiO₂ heterostructures were strongly affected by the thickness of the CNF mat and the carbonization temperatures used in production, which affect the resistance of the CNF mat between the CdS and Pt-TiO₂ sides. The results clearly demonstrated that the CNF acted as an efficient electron-transfer mediator as well as a support material.

© 2016 Elsevier B.V. All rights reserved.

1. Introduction

Photocatalytic water splitting is a promising technology that permits H₂ production directly from water and solar light, which are clean, renewable, and abundant resources [1,2]. Semiconducting photocatalysts have been extensively studied for photocatalytic water splitting [3,4]. In general, multi-component systems are necessary in photocatalytic water splitting to efficiently absorb solar light, separate and transfer photogenerated electron-hole pairs, and catalyze the reduction and oxidation reactions. Many researchers have focused on enhancing the photocatalytic efficiency by developing new semiconducting materials, because low photocatalytic efficiency is a major obstacle for industrial applications of the technology [5–9]. However, cost reduction is also an important factor for industrial applications. Therefore, finding cost-effective materials is necessary for the industrial use of semiconductor-based photocatalytic H₂ production.

Carbon materials have been extensively used for photocatalytic water splitting because they possess special physicochemical properties. Carbon nanomaterials can act as supporting materials with high surface areas [10], catalysts for the reduction reaction [11], and efficient electron-transfer mediators [12–14]. Carbon nanotubes (CNTs) provide spatial confinement for TiO₂ and large surface areas that increase the rates of redox reactions. Two-dimensional graphene sheets in graphene-embedded photocatalysts promote electron transfer by the geometry, built-in electron reservoirs, and excellent charge mobility of graphene. Furthermore, modifications to the graphene surface can improve photocatalytic water splitting by enhancing the light absorption of TiO₂. Carbon nanofibers (CNFs) have useful characteristics including relatively simple fabrication, cost effectiveness, and flexibility [15,16]. Previous studies have shown the advantages of CNFs applied in composites with photocatalytic materials [17–20]. CNFs could enhance photogenerated charge separation, as they have large surface areas and good conductivities.

Previously, we studied the application of a CNF/photocatalyst composite in photocatalytic H₂ production. We first applied a flexible mat of CNFs for H₂ production under UV irradiation [21]. We further investigated the fabrication of CdS and CNF mats and applied this composite to visible light-induced H₂ production [22].

* Corresponding author.

E-mail address: sh2358@dgist.ac.kr (S. Kim).

In the CdS/CNF composite, most electrons reacted with water molecules to generate H_2 on the surface of CdS. However, it was possible that some electrons were transferred to the CNF mat, which would promote electron-hole pair separation; this implies that the CNF mat could function as an electron-transfer mediator as well as a support material. Therefore, to better understand the photocatalytic H_2 production system of CNF/photocatalysts, the role of CNF must be further investigated.

In this study, to investigate the role of CNF, we fabricated a trilayer heterostructure of CdS/CNF mat/Pt-nanoparticle-deposited TiO_2 (Pt- TiO_2) composite. The CNF mats were prepared by electrospinning and carbonization. CdS and Pt- TiO_2 were deposited on the front and back, respectively, of the CNF mat. CdS on the front could directly absorb the visible light and Pt- TiO_2 on the back could act as co-catalyst for H_2 production. Because the Pt particle deposited on the TiO_2 are on the back side, the visible light absorption of Pt- TiO_2 due to surface plasmon resonance (SPR) effects of Pt nanoparticles might be negligible and the effects of depositing Pt- TiO_2 on the back of the CNF mat would help to elucidate the photogenerated electron transfer occurring in the heterostructure. We studied the effects of varying the CNF mat thickness and the carbonization temperature, because these two factors could affect the resistance of the CNF mat and thus the electron-transfer process.

2. Experimental details

2.1. Materials

We used chloroplatinic acid hexahydrate ($H_2PtCl_6 \cdot 6H_2O$, $\geq 37.50\%$ Pt basis, Sigma-Aldrich), titanium oxide (TiO_2 , Degussa), cadmium acetate dihydrate ($CdAc \cdot 2H_2O$, 99%, Sigma-Aldrich), sodium sulfide pentahydrate ($Na_2S \cdot 5H_2O$, 98%, Daejung), sodium sulfite (Na_2SO_3 , 98%, Daejung), polyacrylonitrile (PAN, $M_w = 150000$, Sigma-Aldrich), *N,N*-dimethylformamide (DMF, 99%, Sigma-Aldrich), ethanol (99%, Daejung), methanol (99%, Daejung), nitric acid (HNO_3 , 1 mol/L, Duksan), hydrochloric acid (HCl, 1 mol/L, Duksan) and distilled water to synthesize the samples.

2.2. Preparing CNF with varying thickness

CNF mats were prepared using electrospinning and carbonization, as previously reported [20]. A 10 wt.% PAN solution was prepared by dissolving PAN in DMF and heating the mixture at $85^\circ C$ while stirring for 4 h, followed by cooling to room temperature and stirring for another 12 h. A viscous yellow-brown solution was thus obtained. PAN nanofibers were prepared by electrospinning, in which the PAN solution was fed at a constant rate of $20 \mu L/min$. An electric field of 20 kV was applied, and the distance between the needle and the collector plate was 15 cm. The PAN nanofibers were stacked in different numbers of layers (1, 2, 4, 6, and 8 layers) prior to calcination to control the thickness of the final CNF mats. The collected PAN nanofibers were annealed by raising the temperature at a rate of $5^\circ C/min$ for 50 min and holding at $250^\circ C$ for 20 min under atmospheric conditions, followed by 10 min in N_2 gas. The N_2 gas was in continuous flow. The temperature was raised at a rate of $5^\circ C/min$ for 100 min and held at $750^\circ C$ for another 60 min. Following this, the temperature was raised at $5^\circ C/min$ for 130 min (or 70 min to achieve a carbonizing temperature of $1100^\circ C$) and then held at $1400^\circ C$ (or $1100^\circ C$) for 60 min. The CNF mats were collected after annealing. The obtained samples were acid-treated by submersion in 1 L aqua regia ($HNO_3:HCl = 1:3$ v/v) per g of CNF mat for 30 min [23].

2.3. Preparing trilayer heterostructured CdS/CNF mat/Pt- TiO_2 composite

CdS nanoparticles were fabricated by a precipitation method [24]. Fifty mL 0.2 mM $Na_2S \cdot 5H_2O$ solution was slowly added to 50 mL 0.2 mM CdAc solution with vigorous stirring. Pt- TiO_2 nanoparticles were synthesized through the photodeposition of Pt on the surface of TiO_2 [25]. A stock solution of chloroplatinic acid hexahydrate and 0.5 g/L TiO_2 was briefly dispersed in 10 vol.% methanol with vigorous stirring for 30 min. The Pt: TiO_2 weight ratio was 0.005:1. The suspension color changed from white-yellow to white-gray following irradiation by ultraviolet light for 30 min under N_2 purging gas. The suspension was filtered using $0.45\text{-}\mu m$ polytetrafluoroethylene (PTFE) filters (Millipore) and dried at $80^\circ C$ in an oven.

Trilayer CdS/CNF/Pt- TiO_2 composite structures were synthesized by the doctor blade method. CdS nanoparticles were loaded on one side of the CNF mat by mixing 20 mg of CdS powder with 260 mg of polyethylene glycol solution ($H_2O:PEG = 2:1$ by weight). This CdS paste was loaded with a thickness of $0.48 \mu m$ onto one side of the CNF mat surface using one layer of 3 M tape. After the loading process, calcination was performed at $400^\circ C$ for 30 min, before the CdS-deposited mat was cooled to room temperature. Pt- TiO_2 loading was performed on the other side of CNF by the same process, using as-prepared Pt- TiO_2 instead of CdS.

2.4. Characterization of CdS/CNF/Pt- TiO_2

Scanning electron micrographs were obtained on a field emission scanning electron microscope (FE-SEM) equipped with an energy dispersive X-ray spectrometer (EDS, Hitachi, S 4800). The electrical conductivities of the samples were analyzed by a four-point probe (CMT-SR3000, AIT) on samples of $1\text{ cm} \times 1\text{ cm}$ in size to determine the relationship between electrical conductivity and annealing temperature. The electrical resistances and calculated conductivities between the CdS and Pt- TiO_2 sides of the trilayer electrode were measured by a digital multimeter. The thickness of the CNF mat was measured using digital Vernier calipers (Mitutoyo, Japan) and the side-view SEM images. X-ray diffraction (XRD) patterns were obtained with an X-ray diffractometer (Panalytical, Empyrean, 40 kV, 30 mA) using $Cu-K\alpha_1$ radiation ($\lambda = 1.54178 \text{ \AA}$) and a quartz monochromator. Raman spectra of the samples were analyzed by a Raman spectrophotometer (Thermo Scientific, Nicolet Almega XR) in the wavenumber range of $\sim 100\text{--}4000\text{ cm}^{-1}$ using a 532-nm laser. The elemental binding energies and oxidation states were determined using an X-ray photoelectron spectroscopy (XPS, Thermo Fisher Scientific, Theta Probe AR-XPS System) fitted with a monochromated Al $K\alpha$ source ($h\nu = 1486.6\text{ eV}$).

2.5. Photocatalytic H_2 production and photocurrent measurement

The photocatalytic H_2 production was determined experimentally using two sacrificial reagents of 0.1 M Na_2S and Na_2SO_3 in distilled water. The rectangular quartz reactor held 4 mL of reagent and was similar to the cell used for analysis in UV-vis spectrophotometry. The head volume was 2.4 cm^3 . All samples were formed as $3\text{ cm} \times 0.5\text{ cm}$ rectangular mats with weights of $\sim 38\text{ mg}$. The light source was a 150-W Xe arc lamp (Abet Technologies) with a 420-nm cutoff filter. The distance between the reactor and light source was 15 cm. N_2 gas was bubbled through the reagents for 30 min before irradiation. The H_2 produced was inspected every 30 min for 3 h using a gas chromatograph (GC, HP6890, Agilent) equipped with a thermal conductivity detector (TCD). A photocurrent measurement was performed with a three-electrode system in a 1 M Na_2SO_3 buffer (pH = 12). The working electrode is CdS/CNF/Pt- TiO_2 .

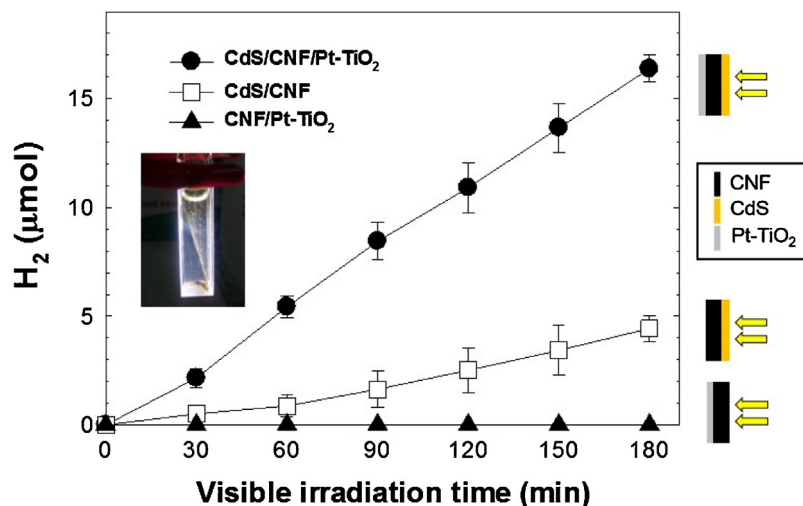


Fig. 1. Time-profiled H₂ production of CdS/CNF/Pt-TiO₂, CdS/CNF, and CNF/Pt-TiO₂ with visible light irradiation ($\lambda > 420$ nm).

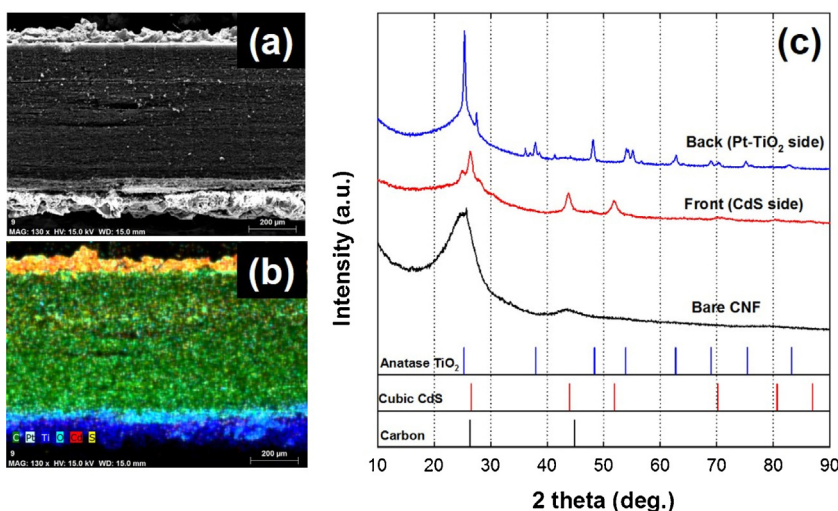


Fig. 2. (a) Cross-sectional SEM image and (b) EDX elemental mapping of CdS/CNF/Pt-TiO₂ composite. (c) XRD patterns of bare CNF and front and back sides of CdS/CNF/Pt-TiO₂ composite.

(0.5 cm × 1.5 cm), which is attached to the Cu tape. The reference electrode and counter electrode are Ag/AgCl and Pt wire, respectively. N₂ was continuously purged before and during photocurrent measurement, and a constant potential (0.2 V vs. Ag/AgCl) was applied to the working electrode using a potentiostat (VSP, Princeton Applied Research). Photocurrent generations were measured under visible light irradiation ($\lambda > 420$ nm) [26].

3. Results and discussion

The photocatalytic H₂ production of the mats was evaluated and compared under visible ($\lambda > 420$ nm) light irradiation. Fig. 1 shows the time profiles of H₂ production on tri- or bilayer heterostructured CdS/CNF/Pt-TiO₂, CdS/CNF, or CNF/Pt-TiO₂. Illustrations of the visible irradiation of CdS/CNF/Pt-TiO₂, CdS/CNF, and CNF/Pt-TiO₂ are also shown in Fig. 1. The trilayer CdS/CNF/Pt-TiO₂ structure produces H₂ at 16.34 μmol for 3 h. Using the bilayer CdS/CNF, H₂ is produced at 4.85 μmol for 3 h, but with CNF/Pt-TiO₂, no H₂ is produced. The trilayer CdS/CNF/Pt-TiO₂ composite structure shows drastically enhanced H₂ production approximately 3.4 times higher than that of the bilayer CdS/CNF. This increase seems to result from the Pt-TiO₂ layer promoting the electron-transfer reaction for H₂

production on the back side of the CNF mat, which suggests that the CNF acts as an efficient electron-transfer mediator. In both bilayer and trilayer structures, CdS acts only as a light absorber. Photogenerated electrons in the conduction band of CdS could be transferred to the CNF mat, or directly react with H⁺ to produce H₂. H₂ production could also occur on the surface of the CNF mat because of the catalytic properties of CNF, as previously reported [27]. With the Pt-TiO₂ layer added to the CNF mat, the transfer of photogenerated electrons might be promoted, corresponding to an obvious reduction in the charge recombination in the CdS layer, which could enhance H₂ production. Therefore, the photocatalytic H₂ production could occur efficiently on trilayer CdS/CNF/Pt-TiO₂ composite heterostructures; CdS, the CNF mat, and Pt-TiO₂ could act as a visible light absorber, electron-transfer mediator, and catalyst for H₂ production, respectively.

We observed cross-sectional SEM images and analyzed the elemental composition of the trilayer CdS/CNF/Pt-TiO₂ heterostructure by EDS mapping, as shown in Fig. 2a and b. Each layer was well formed and easily distinguishable from the others. The thicknesses of the CdS, CNF, and Pt-TiO₂ layers are 100, 500 ~ 600, and 200 μm, respectively. The crystalline structures of CdS, Pt-TiO₂, and CNF are also observed. Fig. 2c shows the X-ray diffraction pat-

Table 1
Electrical conductivity and resistivity values of CNF.

Temperature (°C)	Resistivity (Ω cm)	Conductivity (S/m)
1100	5.325×10^{-2}	1.878×10^3
1400	1.395×10^{-2}	7.171×10^3

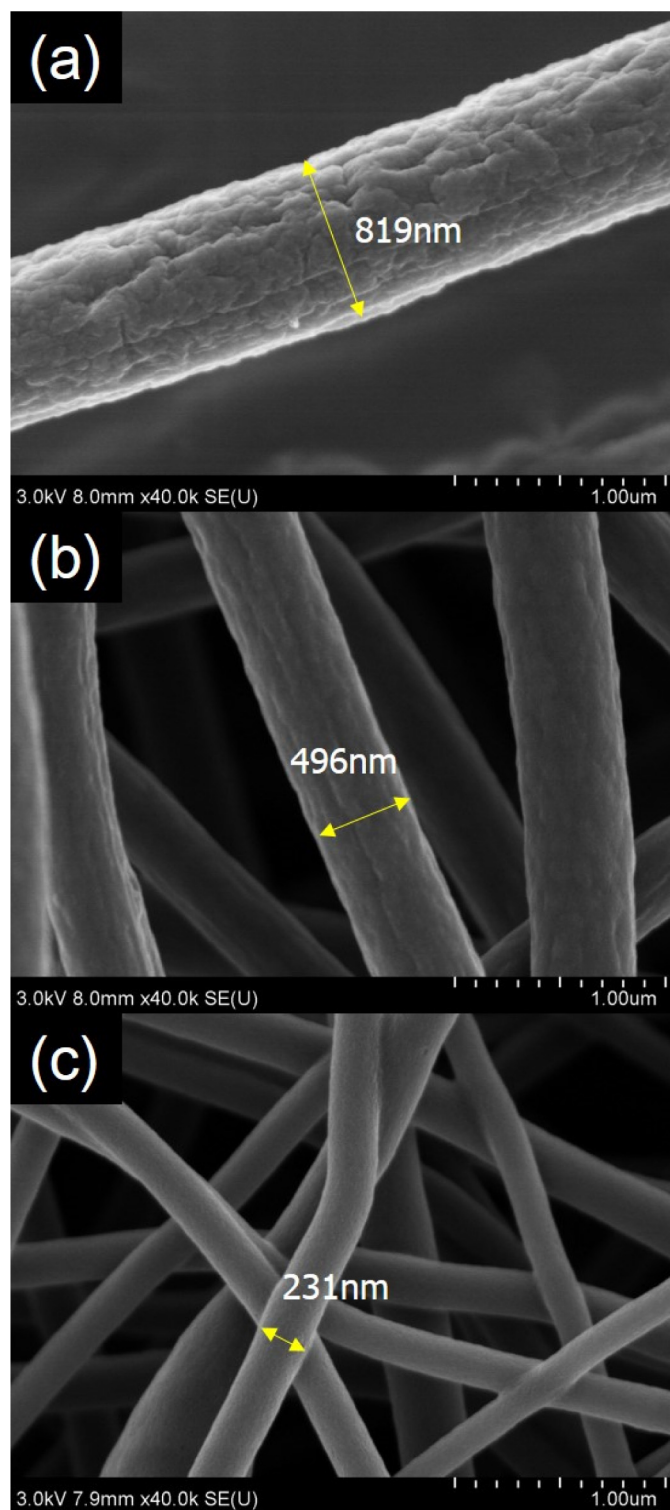
Table 2
 I_D/I_G ratio and FWHM of G band of CNF.

Temperature (°C)	Integrated intensity of D band	Integrated intensity of G band	I_D/I_G	FWHM of G band
1100	2450	1225	2.00	94.08
1400	2419	1332	1.82	78.35

terns of each side of the trilayer CdS/CNF/Pt-TiO₂ heterostructure and of the CNF mat alone. In the pattern from the CdS side, peaks correlating to the (111), (220), and (311) planes of cubic CdS are observed. For the Pt-TiO₂ side, the peaks indicate mixed structures of anatase and rutile TiO₂, which is attributed to the Degussa P25 TiO₂. The crystalline phase of Pt is not observed, which may result from the low content of Pt nanoparticles on the TiO₂. Both the CdS and Pt-TiO₂ side XRD patterns show peaks corresponding to the carbon structure of CNF. This implies that the CdS and Pt-TiO₂ nanoparticles are well-deposited on each side of the CNF mat.

In the trilayer CdS/CNF/Pt-TiO₂ composite structure, CNF does function as an electron-transfer mediator, as shown in Fig. 1. Therefore, the electrochemical properties of CNF are important in the performance of the electrode. A linear correlation was previously reported between the annealing temperatures and electrical conductivities of carbon materials [28]. The carbonization temperatures could strongly influence the electrochemical properties of the CNF mats. To investigate the effects of the carbonization temperature, electrospun PAN nanofibers were carbonized at either 1100 °C or 1400 °C and the properties of the resulting mats were compared. Fig. 3 shows SEM images of the electrospun PAN nanofibers and the CNF mats carbonized at both 1100 °C and 1400 °C. The PAN nanofibers and CNFs both have smooth surfaces. The diameters are approximately 800, 500, and 200 nm for the PAN nanofiber, CNF calcined at 1100 °C, and CNF calcined at 1400 °C, respectively. The diameters of the nanofibers are drastically reduced by carbonization and strongly affected by the carbonization temperature. The higher carbonization temperature forms denser CNF mats. The electrical conductivities of the CNF mats were measured using the four-point probe method to investigate the effect of the carbonization temperature, as described in Section 2.4. The surface resistances and conductivities of the CNF mats are shown in Table 1. The electrical conductivity of CNF increases with increased carbonization temperature. The CNF mat carbonized at 1400 °C has a much higher conductivity than that carbonized at 1100 °C.

These results are explained by Raman analysis, as shown in Fig. 4a, Fig. S1, and Table 2. As shown in Fig. S1, after background subtraction, the Raman spectra were deconvoluted into two peaks centered at ~ 1350 cm⁻¹ and ~ 1580 cm⁻¹ corresponding to the D and G bands, respectively [29]. The D and G bands are associated with the vibrations of sp² carbon atoms with dangling bonds; the integrated intensity ratio (I_D/I_G) corresponds to the level of disorder in the CNF mat. Lower values of I_D/I_G and the full width at half-maximum (FWHM) of the G band indicate more ordered graphitic structures [30]. The I_D/I_G ratios for the CNF mats carbonized at 1400 °C and 1100 °C are 1.82 and 2.00, respectively, and the G band of the CNF carbonized at 1400 °C is narrower than that of the CNF carbonized at 1100 °C, as shown in Table 2. XPS analyses are also used to estimate the quality of the graphitic structure, as shown in Fig. 4b. C 1s peaks are deconvoluted, with results shown in Fig. S2 and Table 3. The peaks observed at 284.5, 285.5, and 290.9 eV

**Fig. 3.** SEM images of (a) electrospun PAN nanofiber webs, and CNF carbonized at (b) 1100 °C and (c) 1400 °C.**Table 3**

XPS C 1s peak positions, FWHM values, and area ratios of deconvoluted peaks of CNFs.

Samples	CNF carbonized at 1100 °C			CNF carbonized at 1400 °C		
	sp ²	sp ³	$\pi-\pi^*$	sp ²	sp ³	$\pi-\pi^*$
Position (eV)	284.5	285.5	290.9	284.5	285.5	290.9
FWHM	0.95	1.47	4.47	0.83	1.79	3.71
Area ratio (%)	48.86	39.99	11.15	61.61	26.74	11.65

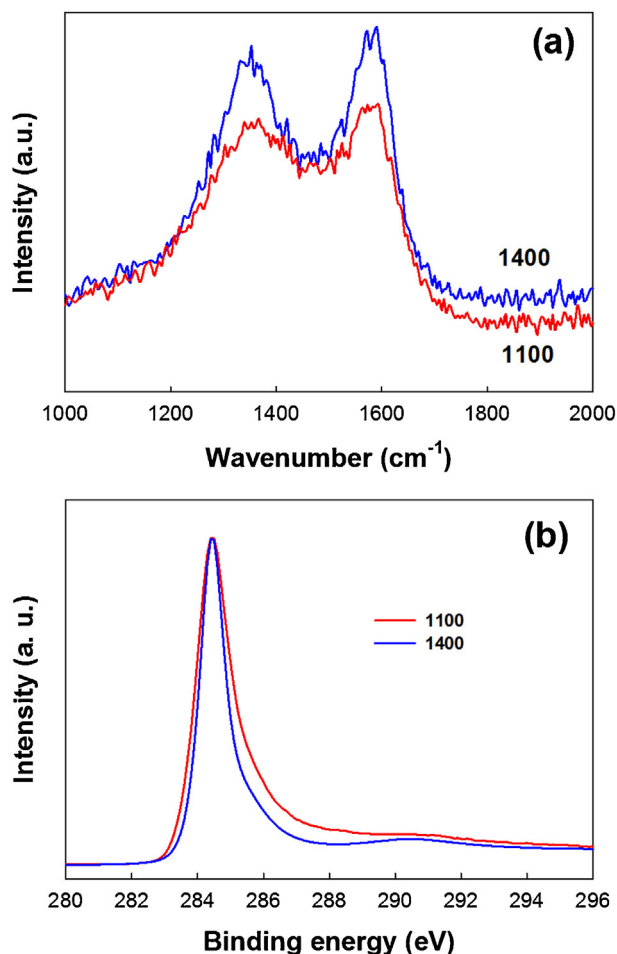


Fig. 4. (a) Raman and (b) XPS C 1s spectra of CNF with different carbonization temperatures.

are attributed to sp^2 , sp^3 , and $\pi-\pi^*$ transitions, respectively [31]. The sp^2/sp^3 ratio increases with increasing the carbonization temperature from 1100 °C to 1400 °C, indicating that the quality of the graphitic structure increases with carbonization temperature. These results suggest that the CNF carbonized at 1400 °C has a higher-quality graphitic structure and higher crystallinity compared to the CNF carbonized at 1100 °C. It has been well known that graphitic carbon has higher conductivity than amorphous carbon [31]. Therefore, the CNF mat carbonized at 1400 °C exhibits higher conductivity.

In the trilayer CdS/CNF/Pt-TiO₂ composite, the electrons are transferred from CdS to Pt-TiO₂ through the resistance between CdS and Pt-TiO₂, which may strongly correlate to the conductivity of the CNF mat. Therefore, it was expected from the electrical conductivities shown in Fig. 4 that the resistance of the CNF mat carbonized at 1100 °C would be much higher than that of the mat carbonized at 1400 °C. The CNF thickness could also affect the transfer of photogenerated electrons from CdS to Pt-TiO₂, which might affect the efficiency of visible light-induced H₂ production. To investigate the effects of varied CNF mat thicknesses as well as those of the carbonization temperatures, the CNF mat thicknesses were controlled by changing the folding number of the electrospun PAN nanofibers before the carbonization procedure. The resistance between the CdS and Pt-TiO₂ sides ($R_{CdS/Pt}$) was measured for all samples (Table 4). The CNF mat thicknesses were measured by SEM cross-sectional images, as shown in Fig. S3 and Fig. S4 for the CNF mats carbonized at 1100 °C and 1400 °C, respectively. Fig. 5 plots $R_{CdS/Pt}$ as a function of the CNF mat thickness.

Table 4

Electrical through-plane resistance values of CNF mats at varied thicknesses.

CNF carbonized at 1100 °C		CNF carbonized at 1400 °C	
Thickness (μm)	Resistance (Ω)	Thickness (μm)	Resistance (Ω)
124	8.2	183	2.1
175	10.2	375	2.8
226	7.6	530	3.6
415	10.6	917	4.4
642	13.2	1284	5.2
821	12.3	1467	6.3
1066	13.5	1512	5.7

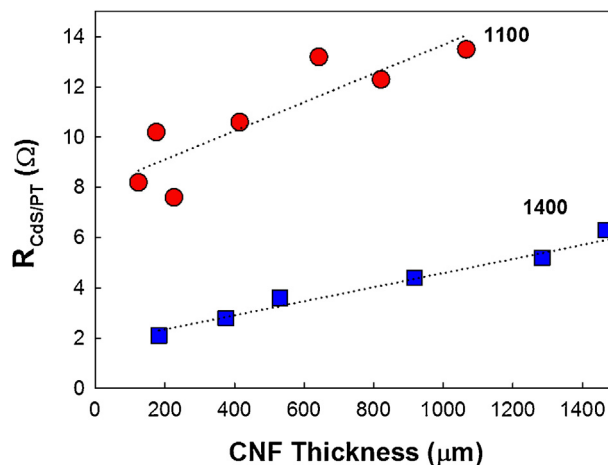


Fig. 5. $R_{CdS/Pt}$ as a function of CNF mat thickness according to the carbonization temperature.

The resistance linearly increases with increasing CNF mat thickness; the slope of increasing resistance is calculated as $\sim 56 \Omega \text{ cm}^{-1}$ and $\sim 31 \Omega \text{ cm}^{-1}$ for CNF mats carbonized at 1100 °C and 1400 °C, respectively. This implies that higher CNF electrical conductivities correlate to weaker dependencies of the resistances on the CNF thicknesses. $R_{CdS/Pt}$ may significantly influence the transfer of photogenerated electrons from CdS to Pt-TiO₂ through the CNF mat in the visible light-irradiated trilayer CdS/CNF/Pt-TiO₂ composite.

In order to investigate the transfer of photogenerated electrons from CdS to Pt-TiO₂, we measure the photocurrent generation in the trilayer CdS/CNF/Pt-TiO₂ composite structure as shown in Fig. 6 and Fig. S5. The results show that the photogenerated electrons of CdS by visible light irradiation ($\lambda > 420 \text{ nm}$) transfer to Pt-TiO₂ through the CNF mats, which were strongly affected by the thickness of CNF and the carbonization temperature. The photocurrent was higher on CNF mats carbonized at 1400 °C than CNF mats carbonized at 1100 °C and decreased with increasing CNF mat thickness. These observations show that photogenerated electrons can cross the CNF mats and the electrical conductivities of CNF and the thickness of CNF mats can influence on the photocurrent generation.

Fig. 7a shows the relationship between CNF thickness and H₂ production in the trilayer CdS/CNF/Pt-TiO₂ composite structures according to the carbonization temperature. The amount of H₂ produced during 3 h irradiation and the time profiles of H₂ production are shown in Fig. S6. When CNF mats of thicknesses below $\sim 300 \mu\text{m}$ are used, the H₂ production was low, despite the electrical conductivities of the thin mats exceeding that of mats thicker than $300 \mu\text{m}$. This implies the existence of an optimum thickness for enhancing the photogenerated electron-hole separation. The electrons accumulated in the CNF mat must overcome interfacial resistance for transfer to the Pt-TiO₂ layer. If the CNF mat is too thin, the photogenerated electron-hole pairs cannot be efficiently separated because of the electrons accumulated in the mat. This means

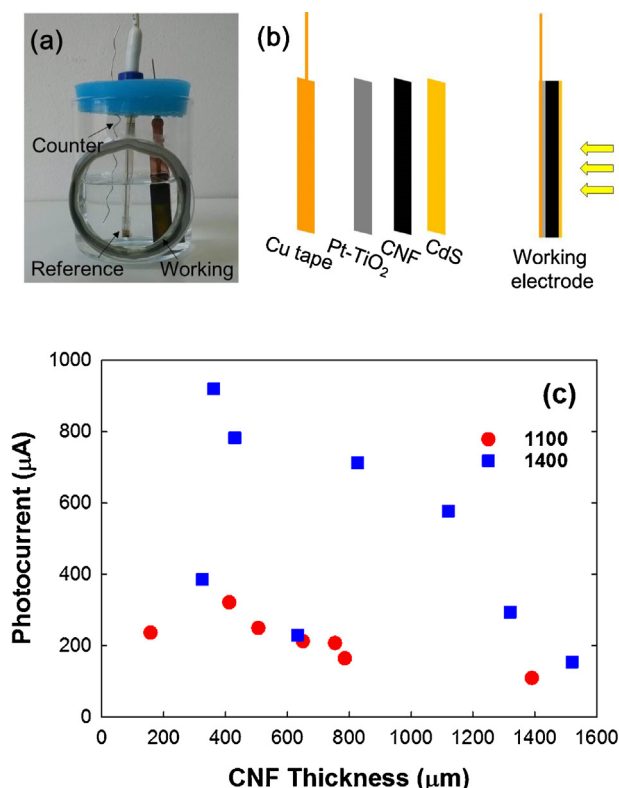


Fig. 6. (a) Picture of the photocurrent measurement set up (b) Schematic illustration of the working electrode (c) Relationship between the photocurrent generation and CNF mat thickness.

that if the rate of photogenerated electron injection from CdS to the CNF mat greatly exceeds the rate of electron drift to Pt-TiO₂, a space charge region forms at the interface between the CNF mat and Pt-TiO₂. In this region, electrons are subject to recombination with holes [32]. The CNF thickness-dependent H₂ production differed significantly with carbonization temperature. The H₂ production on the CdS/CNF/Pt-TiO₂ composite using a CNF mat carbonized at 1400 °C (CdS/CNF1400/Pt-TiO₂) was much higher than that on the CdS/CNF/Pt-TiO₂ composite using a CNF mat carbonized at 1100 °C (CdS/CNF1100/Pt-TiO₂). Moreover, the H₂ production on CdS/CNF1400/Pt-TiO₂ decreased slowly with increasing CNF thickness, while that on CdS/CNF1100/Pt-TiO₂ decreased drastically with increasing CNF thickness. These observations may result from the resistance of the CNF mat. Photogenerated electrons of CdS could be transferred faster to Pt-TiO₂ through a CNF mat with lower resistance. In Fig. 7b, the H₂ production is shown to depend on the calculated $R_{\text{CdS/PT}}$. Using Fig. 5, $R_{\text{CdS/PT}}$ is shown to linearly increase with increasing CNF thickness; thus, equations relating CNF thickness to $R_{\text{CdS/PT}}$ can be obtained. The values of $R_{\text{CdS/PT}}$ for CNF used for H₂ production in Fig. 7a can be calculated; the relationship between H₂ production on CdS/CNF/Pt-TiO₂ and the calculated $R_{\text{CdS/PT}}$ is shown in Fig. 7b. Unless very thin CNF is used, H₂ production on CdS/CNF/Pt-TiO₂ is inversely proportional to $R_{\text{CdS/PT}}$. From these observations, we suggest that the CNF mat acts as an electron-transfer mediator and that $R_{\text{CdS/PT}}$ is a main factor affecting H₂ production by the trilayer CdS/CNF/Pt-TiO₂ composite heterostructure under visible irradiation.

Fig. 8 shows a schematic for visible light-induced H₂ production by the trilayer CdS/CNF/Pt-TiO₂ composite heterostructure, as well as a simplified diagram of the main role of CNF in H₂ production. Electrons are excited by the visible light absorption of the CdS nanoparticles, and electrons and holes are generated in the conduction and valence bands, respectively, of the CdS par-

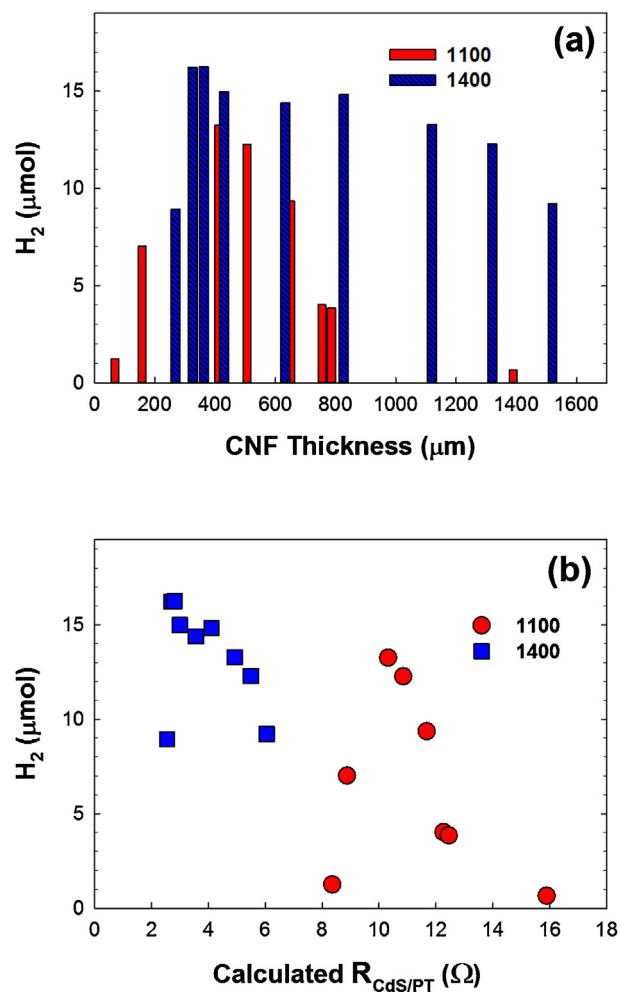


Fig. 7. (a) Relationship between the H₂ production during 3 h irradiation and CNF mat thickness. (b) Correlation of H₂ production with calculated $R_{\text{CdS/PT}}$.

ticles. Some excited electrons react with water molecules and generate H₂ on the surface of CdS; the remaining holes receive electrons from a hole scavenger (Na₂S/Na₂SO₄). The other excited electrons are transferred to Pt-TiO₂ through the CNF mat, which promotes electron-hole pair separation. Therefore, CNF functions as an electron-transfer mediator as well as a support material and $R_{\text{CdS/PT}}$ is a main factor in H₂ production. $R_{\text{CdS/PT}}$ is strongly affected by the carbonization temperature and thickness of the CNF mat utilized in the heterostructured electrode.

4. Conclusions

We fabricated trilayer CdS/CNF/Pt-TiO₂ heterostructures for solar H₂ production by photocatalytic water splitting. Visible light-induced H₂ production was drastically enhanced when Pt-TiO₂ was deposited on the back side of the CNF mat. This implied that the electrons photogenerated by CdS were transported to Pt-TiO₂ through the CNF mat, which promoted electron-hole pair separation, and CNF thus acted as an efficient electron-transfer mediator. The H₂ production of the CdS/CNF/Pt-TiO₂ heterostructures were strongly affected by the electrochemical resistance of the CNF mats, which was controlled by the thickness of the mat and the carbonization temperature used in the preparation of the CNF mat. Therefore, we clearly demonstrated the behavior of the CNF mat as an efficient electron-transfer mediator as well as a support material; the electrochemical conductivity of the CNF mat is thus a main

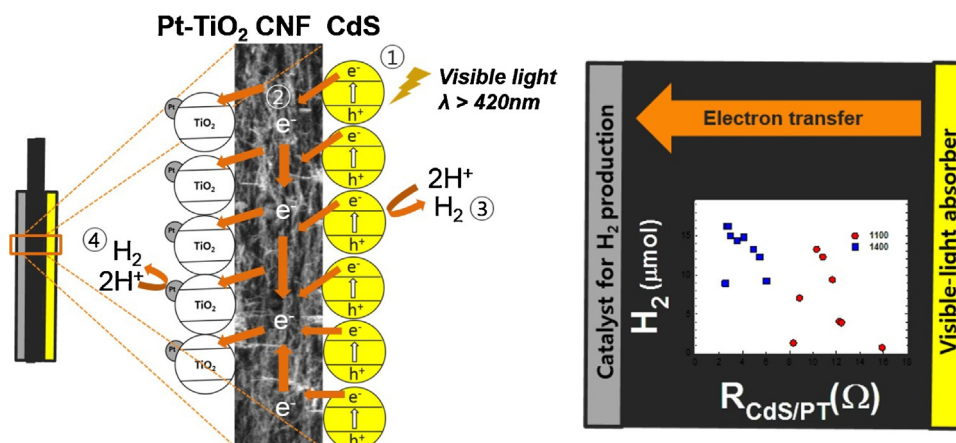


Fig. 8. Schematic for visible light-induced H_2 production of trilayer $CdS/CNF/Pt-TiO_2$ composite heterostructures and simple illustration of electron transfer through CNF.

factor affecting the visible light-induced H_2 production of trilayer $CdS/CNF/Pt-TiO_2$ composite heterostructures. Flexible CNF mats are useful in the practical application of photocatalysts and controlling the electrochemical properties of CNF may be important for the solar H_2 production of photocatalyst-based CNF composites. Furthermore, photocatalyst-based flexible CNF mats have the advantage for the industrial application because the CNF mats are the cost-effective material.

Acknowledgments

This work was supported by the DGIST R&D Program of Ministry of Science, ICT and Future Planning of Korea (16-NB-03).

Appendix A. Supplementary data

Supplementary data associated with this article can be found, in the online version, at <http://dx.doi.org/10.1016/j.apcatb.2016.05.045>.

References

- [1] T. Hisatomi, J. Kubota, K. Domen, *Chem. Soc. Rev.* 43 (2014) 7520–7535.
- [2] J. Ran, J. Zhang, J. Yu, M. Jaroniec, S.Z. Qiao, *Chem. Soc. Rev.* 43 (2014) 7787–7812.
- [3] X. Chen, S. Shen, L. Guo, S.S. Mao, *Chem. Rev.* 110 (2010) 6503–6570.
- [4] W.A. Smith, I.D. Sharp, N.C. Strandwitz, J. Bisquert, *Energy Environ. Sci.* 8 (2015) 2851–2862.
- [5] C. Huang, C. Chen, M. Zhang, L. Lin, X. Ye, S. Lin, M. Antonietti, X. Wang, *Nat. Commun.* 6 (2015) 7698.
- [6] Z.F. Huang, J.J. Song, L. Pan, Z.M. Wang, X.Q. Zhang, J.J. Zou, W.B. Mi, X.W. Zhang, L. Wang, *Nano Energy* 12 (2015) 646–656.
- [7] J. Liu, Y. Liu, N. Liu, Y. Han, X. Zhang, H. Huang, Y. Lifshitz, S.T. Lee, J. Zhong, Z. Kang, *Science* 347 (2015) 970–974.
- [8] W.J. Ong, L.L. Tan, S.P. Chai, S.T. Yong, A.R. Mohamed, *Nano Energy* 13 (2015) 757–770.
- [9] X. Wang, K. Maeda, A. Thomas, K. Takanabe, G. Xin, J.M. Carlsson, K. Domen, M. Antonietti, *Nat. Mater.* 8 (2009) 76–80.
- [10] Q. Xiang, J. Yu, *J. Phys. Chem. Lett.* 4 (2013) 753–759.
- [11] Z. Li, B. Gao, G.Z. Chen, R. Mokaya, S. Sotiropoulos, G.L. Puma, *Appl. Catal. B-Environ.* 110 (2011) 50–57.
- [12] Q. Xiang, J. Yu, M. Jaroniec, *Chem. Soc. Rev.* 41 (2012) 782–796.
- [13] J. Ryu, S. Kim, H.I. Kim, E.H. Jo, Y.K. Kim, M. Kim, H.D. Jang, *Chem. Eng. J.* 262 (2015) 409–416.
- [14] H.I. Kim, S. Kim, J.K. Kang, W. Choi, *J. Catal.* 309 (2014) 49–57.
- [15] M. Inagaki, Y. Yang, F. Kang, *Adv. Mater.* 24 (2012) 2547–2566.
- [16] H.Q. Hou, D.H. Reneker, *Adv. Mater.* 16 (2004) 69–73.
- [17] J. Mu, C. Shao, Z. Guo, Z. Zhang, M. Zhang, P. Zhang, B. Chen, Y. Liu, *ACS Appl. Mater. Interfaces* 3 (2011) 590–596.
- [18] W. Guo, F. Zhang, C. Lin, Z.L. Wang, *Adv. Mater.* 24 (2012) 4761–4764.
- [19] S. Kim, M. Kim, Y.K. Kim, S.-H. Hwang, S.K. Lim, *Appl. Catal. B-Environ.* 148–149 (2014) 170–176.
- [20] S. Kim, S.K. Lim, *Appl. Catal. B-Environ.* 84 (2008) 16–20.
- [21] M. Kim, A. Razzaq, Y.K. Kim, S. Kim, S.I. In, *RSC Adv.* 4 (2014) 51286–51293.
- [22] Y.K. Kim, M. Kim, S.H. Hwang, S.K. Lim, H. Park, S. Kim, *Int. J. Hydrogen Energ.* 40 (2015) 136–145.
- [23] Y.K. Kim, H. Park, *Energy Environ. Sci.* 4 (2011) 685–694.
- [24] H. Park, Y.K. Kim, W. Choi, *J. Phys. Chem. C* 115 (2011) 6141–6148.
- [25] S.K. Choi, S. Kim, S.K. Lim, H. Park, *J. Phys. Chem. C* 114 (2010) 16475–16480.
- [26] S.G. Hickey, D.J. Riley, E.J. Tull, *J. Phys. Chem. B* 104 (2000) 7623–7626.
- [27] G. Khan, S.K. Choi, S. Kim, S.K. Lim, J.S. Jang, H. Park, *Appl. Catal. B-Environ.* 142–143 (2013) 647–653.
- [28] H. Chen, M.B. Muller, K.J. Gilmore, G.G. Wallace, D. Li, *Adv. Mater.* 20 (2008) 3557–.
- [29] Y.W. Zhu, S. Murali, W.W. Cai, X.S. Li, J.W. Suk, J.R. Potts, R.S. Ruoff, *Adv. Mater.* 22 (2010) 3907–3924.
- [30] D. Papkov, A. Goponenko, O.C. Compton, Z. An, A. Moravsky, X.Z. Li, S.T. Nguyen, Y.A. Dzenis, *Adv. Funct. Mater.* 23 (2013) 5763–5770.
- [31] X. Mao, F. Simeon, G.C. Rutledge, T.A. Hatton, *Adv. Mater.* 25 (2013) 1309–1314.
- [32] P.V. Pesavento, K.P. Puntambekar, C.D. Frisbie, J.C. McKeen, P.P. Ruden, *J. Appl. Phys.* 99 (2006) 094504.